Wood Chemistry

Umesh P. Agarwal*, Richard S. Reiner, Carlos Baez and Sally A. Ralph

Native state of wood cellulose: evidence that further supports its non-crystalline nature

https://doi.org/10.1515/hf-2022-0176
Received November 16, 2022; accepted March 10, 2023;
published online March 30, 2023

Abstract: Although highly desirable, the nature of wood-cellulose in its native state has remained difficult to comprehend. Contrary to the traditional acceptance of wood-cellulose being crystalline, in 2016, the authors' research found that the cellulose was not crystalline. Here, additional evidence is presented that further supports the non-crystalline model. One of the key pieces of evidence was obtained by 64% H_2SO_4 hydrolysis of tension- and opposite-aspen woods (TW and OW, respectively). The TW (G-layer rich) yielded significant amount of CNCs (TW-CNCs, 20.7%), the OW yielded a much lower amount (OW-CNCs, 5.4%). Although a higher yield of TW-CNCs was expected due to the presence crystalline cellulose in the G-layer, the lower yield of the OW-CNCs was a surprise because, assuming absence of G-layer, based on the authors' earlier findings no CNCs were expected to be generated. To explain this anomaly, anatomical examination of the woods using stains was carried out which showed that some OW fibers also contained the crystalline G-layer and therefore, provided an explanation as to why the OW-CNCs were produced. The results clearly showed that the acid hydrolysis did not destroy the crystalline cellulose and therefore, in the case of a normal (G-layer free) wood which, as previously reported had not generated CNCs, the cellulose must have been non-crystalline. An additional indication of the wood's S_2 cellulose being not crystalline was the absence of the 93 cm^{-1} Raman band in the low frequency spectrum of the TW S_2 layer. Further evidence was obtained by comparing low frequency Raman spectra of TW-CNCs, TW-holopulp, and aspen-holopulp as well as the mixture-samples of crystalline cellulose and xylan at the concentration levels of their occurrence in these holopulps. Overall, these findings provided further support to the contention that the native wood-cellulose is non-crystalline.

Keywords: cell wall; CNCs; G-layer; Raman spectroscopy; XRD.

***Corresponding author: Umesh P. Agarwal**, Fiber and Chemical Sciences Research, USDA FS, Forest Products Laboratory, 1 Gifford Pinchot Drive, Madison, WI 53726-2398, USA, E-mail: umesh.p.agarwal@usda.gov
Richard S. Reiner and Sally A. Ralph, Fiber and Chemical Sciences Research, USDA FS, Forest Products Laboratory, 1 Gifford Pinchot Drive, Madison, WI 53726-2398, USA
Carlos Baez, Analytical Chemistry and Microscopy Laboratory, USDA FS, Forest Products Laboratory, 1 Gifford Pinchot Drive, Madison, WI 53726-2398, USA

1 Introduction

As a material, from construction to pulp and paper, wood has been used for centuries. It has many useful properties and is renewable and capable of carbon sequestration. The latter is one of the most valuable characteristics that timber provides. Wood, in the never dried state, contains water in addition to cellulose, lignin, and hemicelluloses – the main components. Water has unique influence not only on the properties of green wood but also on the structures of other wood components (Cresswell et al. 2021; Penttila et al. 2020). Nevertheless, water's role in living plant cell walls and how it interacts with cell wall polysaccharide components remains not well understood (Penttila et al. 2020). Moreover, even before water-cellulose interactions can be elucidated, the understanding of cellulose's structure remains complicated. Traditionally, wood cellulose has been considered as a crystalline material (Andersson et al. 2003; Fernandes et al. 2011; Leppanen et al. 2009; Newman et al. 2013) and it has been reported that simulated XRD patterns based on the crystallite size of cellulose can alone explain the diffraction pattern of cellulose materials (Fernandes et al. 2011; French and Cintron 2013; Nam et al. 2016). Recent research has pointed to a situation where the existing model of wood cellulose as being crystalline is no longer valid and instead, a non-crystalline model is likely (Agarwal et al. 2016, 2018). This conclusion was based on the following findings: (a) wood-cellulose in the never-dried native state is laterally aggregated where internal chains are water-accessible, (b) hydroxymethyl groups (CH_2OH) in cellulose exist not only in the *tg* conformation but also in the *gt* rotamer form, (c) in native-state fibrils, low-frequency Raman bands due to cellulose crystal domains are absent, indicating the lack of

crystallinity, (d) failure of the normal 64% H_2SO_4 hydrolysis procedure to produce cellulose nanocrystals from untreated softwood, and (e) deuterated-CNCs could be generated from the hydrothermally treated poplar indicating that cellulose chains were accessible to water and thereby became partly crystalline upon the hydrothermal treatment (Agarwal et al. 2018). Moreover, it was reported that with higher treatment temperature, more crystalline cellulose was produced. If wood-cellulose was already crystalline, that cannot happen. In the context of the present work, the crystalline cellulose is defined as a structure that has a crystal lattice that extends in all directions (translational periodicity) and therefore, having long-range positional order. Moreover, water and most other small molecules cannot get into the crystalline cellulose. Additionally, the work of some other researchers based on six primary grass and *Arabidopsis* cell walls is also relevant where they showed that in the interior of plant primary cell wall microfibrils cellulose has five different conformations and that cellulose ^{13}C NMR chemical shifts differed significantly from the ^{13}C chemical shifts of the Iα and Iβ allomorphs (Wang et al. 2016). And therefore, in the opinion of the authors, such cell wall cellulose cannot be crystalline because, within the fibril, the cellulose conformations and the resulting H-bonding patterns between the chains would be different (Jarvis 2018; Wang et al. 2016). The existence of the above-mentioned different cellulose conformations in the primary wall further supported the results of an earlier study where the primary cell wall microfibrils of celery collenchyma contained extensive disorder in lateral packing, conformation, and hydrogen bonding (Thomas et al. 2013). Even though these microfibrils had extensive disorder, their XRD resembled that of crystalline cellulose (Thomas et al. 2013). This further supported the conclusion that non-crystalline cellulose can contribute in the same XRD region as crystalline cellulose. The understanding of wood-cellulose supramolecular structure is important to numerous fields. For instance, areas such as cellulose biosynthesis, plant growth and function, biorefinery, cellulose nanomaterials, and wood science and technology, in general, would all benefit.

Although wood-cellulose has been studied *in situ* as well as after being isolated, the findings of the investigations are limited because the cellulose supramolecular structure changes depending upon the conditions of isolation (Agarwal et al. 2016, 2021a; Atalla et al. 2017; Ono et al. 2022; Ramanen et al. 2012; Sannigrahi et al. 2008). That is not necessarily the case with some other types of celluloses (e.g., tunicin, algal, bacterial, and cotton) because they are much more crystalline (Agarwal et al. 2018). In this context, interpretation of data from various analytical methods is also not straightforward because, as was reported recently, organized cellulose structures are capable of making contributions in the same spectral/diffraction regions as crystalline cellulose (Agarwal et al. 2021a). Yet another difficulty arises from the fact that although two main phases of cellulose structures, namely, crystalline and amorphous, are widely recognized, defining the intermediate states has proven to be quite challenging. In the absence of that, terms such as paracrystalline, non-crystalline, semi-crystalline, ordered, disordered, organized, and disorganized are often used (Agarwal et al. 2016; Larsson et al. 1997; Penttila et al. 2020; Sannigrahi et al. 2008).

Published literature points to many studies where the obtained results can be better interpreted by invoking a model that is semi-crystalline or non-crystalline. For instance, X-ray diffractogram changes upon drying and rewetting of woods (Hill et al. 2010; Zabler et al. 2010), repeated drying and wetting at 25 °C and hydrothermal treatments lead to the increase in the crystallinity of wood-cellulose (Agarwal et al. 2018; Toba et al. 2013, 2022), effects of cyclic drying and moistening on the mechanical and physical properties of wood (Toba et al. 2022), production of CNCs from pulps (Chen et al. 2015; Moon et al. 2011; Phanthong et al. 2018; van de Ven and Sheikhi 2016; Zhu et al. 2021), and higher NMR- and XRD-crystallinities of cellulose materials in the wet state compared to the values in the dry state (Agarwal et al. 2017, 2021b; Park et al. 2009). Indeed, for wood-pulp derived cellulose nanofibrils (CNFs), existence of alternate crystalline and amorphous regions in cellulose has been reported by direct observation using atomic force microscopy (AFM) (Spiliopoulos et al. 2021) Besides, many unsettled questions/interpretations still need to be elucidated by further research. For example – why is the crystallinity (CrI) of wood-pulp derived sulfated cellulose nanocrystals (SCNCs) not significantly higher than that of the pulp (Moon et al. 2011)? Does the cocrystallization phenomenon really exist (Kontturi et al. 2016; Kuribayashi et al. 2016; Leboucher et al. 2020; Nazhad and Paszner 1994; Newman 2004)? And lastly, although cellulose is biosynthesized in the molecular form, it remains unknown how it becomes crystalline in the plant cell wall (Guerriero et al. 2010). In the case of cocrystallization, actually, evidence that contradicts the existence of the phenomenon exists (Saito et al. 2007). This is because if the fibrils in the bleached kraft pulp, which was used in the TEMPO oxidation, were cocrystallized by the thermochemical treatment, post oxidation, the cocrystallization (in the cellulose nanofibrils) should have been detected. However, that was not the case and only individually separated 3 nm wide pulp fibrils were obtained (Saito et al. 2007). This negated the existence of cocrystallization in the bleached kraft pulp.

Earlier findings of the authors indicated that at the fibrillar level wood cellulose was composed of non-crystalline assembly of cellulose chains and on that basis, a new model of the cellulose was proposed (Agarwal et al. 2016, 2018). In the present study, the authors provide evidence that further supports that finding. One of the several investigations reported here is based on the 64% H_2SO_4 hydrolysis of TW (G-layer rich and hence, contains crystalline cellulose) (Muller et al. 2006; Yamamoto et al. 2010) and OW fibers from aspen wood (*Populus tremuloides*). From the earlier work (Agarwal et al. 2016), one of the questions that needed further study had to do with the ability of 64% H_2SO_4 to destroy crystalline cellulose. This would be specifically answered here because in the CNC production process a crystalline-cellulose containing sample, aspen TW, is being hydrolyzed by the acid. The other experiments were designed so that a comparison of the Raman spectra of aspen wood holopulps and samples of mixtures of crystalline-cellulose and xylan can be carried out. The latter were prepared with known amounts of cotton microcrystalline cellulose (MCC) and xylan such that their concentrations were similar to what existed in the wood holopulps (after considering residual lignin and non-cellulosic polysaccharides as xylan). In these spectra, particular attention was paid to the presence or absence of the Raman bands at 172 and 93 cm^{-1}, both of which are known to arise from crystalline cellulose (Agarwal 2014; Agarwal et al. 2016, 2018).

2 Materials and methods

2.1 Chemicals

NaOH (AR grade) and sodium chlorite (technical grade) were obtained from Sigma–Aldrich (St. Louis, MO) or Alfa Aesar (Tewksbury, MA). Sulfuric acid (Certified ACS plus, 96% assay) and acetic acid glacial were from Fisher Scientific (Pittsburg, PA). Xylan was acquired from Sigma–Aldrich (St. Louis, MO). All other chemicals and reagents, unless stated otherwise, were purchased from Sigma–Aldrich (St. Louis, MO).

2.2 Cellulose and other samples

Cotton MCC (microcrystalline cellulose) Whatman CC31 powder was from Whatman International Ltd. (Maidstone, UK). Aspen wood (*P. tremuloides*) and reaction aspen wood (TW and OW) were available at Forest Products Laboratory, Madison WI. Softwood bleached kraft pulp (SWBKP) was obtained from NewPage Corporation, Miamisburg, Ohio. Aspen holopulp was the same as used in the earlier studies from where further details can be obtained (Agarwal et al. 2013, 2016). Similarly, aspen holopulp was obtained by using the standard methods described earlier (Agarwal et al. 2013). Kraft pulp CNCs were the same as previously analyzed (Agarwal et al. 2021b). Amorphous cellulose was prepared from cotton MCC using the method reported previously where the MCC was ball-milled for 2 h (Agarwal et al. 2010). For Raman analysis, mixtures of cotton MCC and xylan powders were prepared. In these mixtures MCC:xylan wt. ratios varied from 90:10 to 10:90.

2.3 Holopulps and CNCs from reaction and opposite woods

From aspen branch wood, TW and OW wood regions were isolated by sawing and the samples were ground, using a Wiley mill, to 40 mesh. Wiley milling does not cause any change in the crystallinity of wood (Agarwal et al. 2014). The methods, described below, were used to prepare holopulps and CNCs from both TW and OW woods. The wood powders were extracted with acetone/water (9:1) and air dried. Air-dried milled wood (52.5 g) was placed in a 5 L round-bottom flask with 1 L of water. Vacuum was pulled and released several times to ensure the wood meal was fully wetted. Another 0.6 L of water was added to rinse down the sides of the flask. Mechanical stirring was started, and the flask was placed in a 70 °C water bath for one-half hour to equilibrate to the bath temperature. To produce holopulp from wood, $NaClO_2$ and CH_3COOH were added periodically, starting with 20 g of $NaClO_2$ and 6 mL of CH_3COOH and subsequently, for the next 2 h, adding equivalent amounts of the chemicals hourly. Thereafter, starting at the 3rd hour, these amounts were reduced to 7.5 g of $NaClO_2$ and 3 mL of CH_3COOH and the additions were continued for the next 3 h. After the last hour of the treatment, the solution was cooled on ice for 30 min. The bleached wood meal (holopulp) was filtered and washed, frozen overnight, and then freeze-dried.

Freeze-dried holopulp (35 g) was placed in a 1 L round-bottom flask equipped with a mechanical stirrer. The flask was evacuated and refilled with nitrogen once. The flask was evacuated again and 280 mL of 64 wt% H_2SO_4 was added while mixing the holopulp. The flask was filled with nitrogen and placed in a 45 °C water bath for 120 min with mixing. At the end of the acid treatment, the hydrolysis reaction was quenched by diluting it to 2 L with water. The suspension color was bleached by adding one gram of $NaClO_2$ to the acidic CNC suspension over one-half hour. Then, approximately 1.5 L of a 7.5 wt% NaOH solution was used to neutralize the suspension to pH 7. The suspension was topped off to 4.5 L and allowed to settle overnight. After decanting approximately 3.5 L of the clear liquid, the remaining suspension was concentrated by centrifugation at 5000 G for 15 min. The solids were diluted and placed in a Spectra-por five membrane (12–14 kDa MWCO) and dialyzed against DI water for 1 week (TW-CNCs) to 10 days (OW-CNCs). The molecular weight-cutoff (MWCO) of the membrane implied that the CNCs, which have a molecular wt. significantly >90 kDa would not at all diffuse across the membrane. The suspension was centrifuged at 5000 G for 15 min. The colloidal CNCs were decanted and concentrated on a rotovap. A sample of the concentrated suspension was frozen and freeze-dried.

2.4 AFM imaging

The TW- and OW-CNCs were analyzed by AFM. The starting CNC stock (1.0 wt%) was diluted to 0.001 wt% and then manually tumbled in an Erlenmeyer flask to promote particle dispersion. Use of a magnetic stirrer was avoided to minimize the possibility of sample contamination. In addition, some of the sample aliquots were sonicated for 1.5 h in a water bath to help further disperse any agglomerates. Then, a drop of

the 0.001 wt% CNC suspension was deposited on a freshly cleaved mica surface and left to air dry. Next, AFM images were obtained using the TT-AFM (AFMWorkshop, Hilton Head Island, SC) equipped with the 15 µm scanner. The authors collected a total of 20 images per sample. The half of the images were measured using a scan size of 10 µm and the other half using a scan size of 5 µm. The scanning rate was always 0.6 Hz, and the image resolution was also kept constant at 512 pixels by 512 pixels.

Custom-written scripts in Mathematica 12.1 (Wolfram Research, Champaign, IL) were used to level the resulting topographical images. First, image leveling was performed utilizing a combination of 2D polynomial, mean value line-leveling, and background estimation functions to approximate the background while minimizing overfitting. Next, individual particles were identified using pixel connectivity after applying leveling functions and using binary segmentation. Image segmentation was performed manually by intensity thresholding to separate the background from the foreground (particles). Once the particle identification and labeling were complete, statistical analysis was performed to obtain parameters such as max particle height, mean particle height, and particle length.

2.5 Compositional analysis

Various types of aspen woods (TW and OW) and aspen holopulps (TW-, OW-, and aspen-holopulps), SWBKP, and cotton MCC samples were analyzed for chemical composition. The amount of Klason lignin and carbohydrates (glucan, xylan, mannan, arabinan, and galactan) were determined using previously published methods (Davis 1998; Tappi test method 1983). Reproducibility for Klason lignin was 0.4%, and for the carbohydrate analysis, the standard deviation was <1% of assayed sugar (Davis 1998).

2.6 Anatomical observations of woods

Transverse sections (24 µm in thickness) from TW and OW were cut with a sliding microtome, counterstained with 1:1 aqueous safranin O and Alcian Blue, destained in 70% ethanol, then mounted in a 1:1 solution of glycerin and 95% ethanol. Slides were heated at ~120 °C for at least 3–5 min, then cooled and later observed using brightfield transmitted light microscopy. Between the destaining and heating, some loss of safranin staining is expected. Additionally, one 24 µm transverse section was also stained using aqueous safranin O.

2.7 Confocal Raman microscopy

A Raman microprobe spectrometer, LabRam HR Evolution (Horiba Jobin Yvon, Edison, NJ, USA) was used in the present study. This spectrometer is equipped with a confocal microscope (Olympus U-5RE-2), a piezoelectric x, y stage, three lasers (532, 633, 785 nm) and a CCD detector. Using a 633-nm laser, Raman spectra from various morphological regions (e.g., G-layer and S_2) of 30 µm thick X-sections of TW were obtained. For sampling purposes, the TW section was extracted with ethanol:water (9:1) and dried under ambient conditions. Subsequently, the section was mounted on a 1.27 cm diameter Scotch® double stick clear dot (3M St. Paul, MN) whose one side was first attached to a microscope glass slide. With the 100× objective, the lateral resolution was 0.8 µm. To get better signal-to-noise ratio, 10 spectra, each of 15 s duration were averaged at each sampled location. In the TW section, many S_2 and G-layers, and within each of them several locations, were sampled. The spectra reported here are typical of these analyzed regions.

2.8 FT-Raman spectroscopy and cellulose crystallinity calculations

Samples were analyzed, in triplicate, with a Bruker MultiRam spectrometer (Bruker Instruments Inc. Billerica, MA). The Raman system is equipped with a 1064 nm 1000 mW continuous wave (CW) diode pumped Nd:YAG laser. Approximately 100 mg dry powder of each sample was pressed into a pellet (using ~276 × 10^6 dyn/cm^2 of compressive pressure from a hydraulic press) and three Raman spectra were recorded from different pellet locations using 600 mW laser power. To obtain good signal-to-noise ratio, 2048 scans were averaged.

Bruker OPUS 7.2 software was used to determine peak positions and process the spectral data. The processing of spectra involved background removal, normalization at 1096 cm^{-1}, and various mathematical operations. Background correction was performed using the "rubberband option" in OPUS using 64 baseline points. For plotting purposes, the spectra were converted to ASCII format which then allowed the spectral data to be exported to Excel.

Cellulose CrI was estimated using previously reported Raman methods – 380-Raman and 93-Raman (Agarwal et al. 2010, 2016, 2018). The following two equations were used to estimate the CrIs.

$$\mathrm{Cr}I_{380\text{–Raman}} = \frac{\left(\left(\frac{(I_{380}/I_{1096}-0.0286)}{0.0065}\right)+2.0212\right)}{0.8222} \quad (1)$$

$$\mathrm{Cr}I_{93\text{–Raman}} = \frac{\left(\frac{I_{93}}{I_{1096}}\right)-0.0182}{0.0029} \quad (2)$$

where in the equations I_{93}, I_{380}, and I_{1096} are, respectively, band intensities at 93, 380, and 1096 cm^{-1} in the spectra of the cellulose-containing samples.

2.9 X-ray diffraction and Segal-WAXS CrI calculation

Wide-angle X-ray diffraction (XRD) profiles were recorded in the reflection mode on a Bruker D8 Discover diffractometer with monochromatic CuK_α (λ = 1.5418 Å) point source and a VÅNTEC-500 detector at the Materials Research Science and Engineering Center, University of Wisconsin, Madison. The X-ray diffractometer beam aperture of 0.5 mm was used. In all cases, diffractograms were obtained on the sample pellets after the acquisition of the Raman spectra. Both sides of the pellet were sampled and the average values of the Segal-WAXS CrIs are reported. The CrIs were calculated by measuring (200) peak intensity, I_{200}, and subtracting the amorphous contribution, I_{am}, at approximately 2θ = 18° (Equation (3)) (Segal et al. 1959).

$$\mathrm{Cr}I = 100 * (I_{200} - I_{am})/I_{200} \quad (3)$$

3 Results and discussion

3.1 Crystalline nature of G-layer

Figure 1 shows optical microscopic image of TW cross-section showing fibers with visible gelatinous layers and vessels in part with tyloses. From this image, the presence of G-layer can be easily discerned which, in the fibers, occurs in lieu of S_3. The G-layer partially replaces the second layer

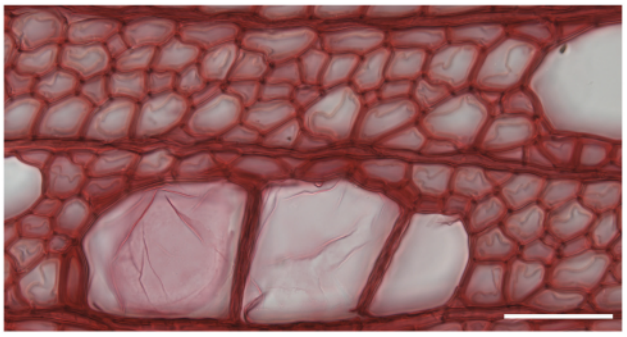

Figure 1: Transmitted light micrograph of a transverse section of *Populus tremuloides* stained with safranin O, showing fibers with conspicuous gelatinous layers and vessels in part with tyloses. Scale bar: 200 µm.

of secondary walls (S_2 layer) (Mellerowicz et al. 2001). In Figure 1, in several places, the G-layer appears broken/separated from S_2 which is an artifact of drying/sectioning. Various cell wall morphological regions – G-layer, S_2 and compound middle lamella (CmL), were investigated by confocal Raman spectroscopy (spatial resolution ~0.8 µm) (Agarwal 2006). The typical G-layer spectrum, in the region 70–1700 cm^{-1}, is reported in Figure 2 along with spectra of a neighboring S_2 region in the cell wall and of MCC (highly crystalline). Upon comparison (Figure 2), it can be noted that, in the spectrum of S_2, a peak of cellulose at 93 cm^{-1} is absent while the contribution of lignin at 1600 cm^{-1} is present. Because the 93 cm^{-1} feature is an aspect of crystalline cellulose, this suggested that S_2 cellulose is unlikely to be crystalline. Moreover, the spectra of G-layer and MCC (Segal CrI 89.7%) were very similar (Figure 2) and both contained the peak at 93 cm^{-1}, indicating that the former was composed of highly crystalline cellulose (Agarwal et al. 2018). Previously, the contributions at 93, 172, and 380 cm^{-1} have been reported to be due to cellulose crystals (Agarwal et al. 2014, 2018). Additionally, it has been reported that the 93 cm^{-1} band, assigned to rotation of cellulose molecule (Makarem et al. 2019), is capable of distinguishing between the crystalline and organized (but not-crystalline) phases of cellulose (Agarwal et al. 2018). This low energy band of crystalline cellulose has also been detected by another type of spectroscopy, terahertz spectroscopy (Vieira and Pasquini 2014; Wang et al. 2021), where lattice modes of organic molecules and polymers are usually detected (Funaki et al. 2017; Parrott and Zeitler 2015). 93 cm^{-1} wavenumber corresponds to 2.8 THz and is detected in that region in terahertz spectroscopy. In any case, the aspect that G-layer is composed of almost pure crystalline cellulose, is extensively documented (Dadswell and Wardrop 1955; Muller et al. 2006; Pilate et al. 2004; Wada et al. 1995). This is also supported by the spectra in Figure 2 where the Raman spectra of S_2, G-layer, and MCC in 70–1700 cm^{-1} region are compared. It needs to be noted that in the S_2 spectrum, in addition to the contributions of cellulose, contributions of aspen lignin are present at 1661, 1595, 1455, 1331, 1130, 1037, 598, 531, and 369 cm^{-1} which were not detected in the spectra of the cotton and G-layer (Agarwal 2006; Agarwal et al. 2011). In this spectrum (Figure 2), the syringyl-lignin contribution at 369 cm^{-1} makes the 380 cm^{-1} cellulose peak broader on the low frequency side compared to the widths of this peak in the G-layer and MCC spectra.

3.2 Production of CNCs

The yields of the CNCs obtained from similar amounts of TW- and OW-holopulps are listed in Table 1. In all probability, TW-CNCs (yield 20.7%, Table 1) came from the G-layer because normal cell wall cellulose in known to produce no CNCs (Agarwal et al. 2016). Compared to the TW-holopulp, the amount of CNCs produced by the OW-holopulp (5.4%, Table 1) was 74% lower. Moreover, chemical composition analysis (Table 2) indicated that compared to the TW-holopulp the amount of glucan in the OW-holopulp was 20% lower. Accordingly, accounting for this difference, the yield from the opposite wood (or holopulp) should have been 16.6%, instead of 5.4% (Table 1). However, this assumes no difference in the capability of the two types of cell wall celluloses to produce CNCs. Nevertheless, considering the fact that CNCs can only be produced from crystalline cellulose (and therefore, G-layer) but not from the other wood cell walls and that the OW-holopulp (or OW) is not supposed to have any G-layer according to the literature (Coutand et al. 2004; Gao et al. 2021; Mellerowicz et al. 2008), production of the CNCs from OW-holopulp was not expected. Therefore, how does one explain the generation of the OW-CNCs? To answer this question, an anatomical analysis of the TW and OW was carried out (see below). The investigation revealed that G-layer existed in the OW, albeit sparingly, accounting for the low amount of CNCs production from this wood.

The AFM images of the TW- and OW-CNCs are shown, respectively, in Figures 3A and B. These CNCs along with the SWBKP CNCs (pulp-CNCs) were analyzed, and the data are listed in Table 1. Based on the mean particle height, it appears that compared to the TW-CNCs (4.0 nm), the OW-CNCs (3.1 nm) were slightly smaller in height/width, but both types had heights that were similar to the pulp-CNCs (Table 1). In AFM, the height measurements are considered to be quite precise and therefore, for CNCs, assuming a square cross-section, are taken as representation of their widths.

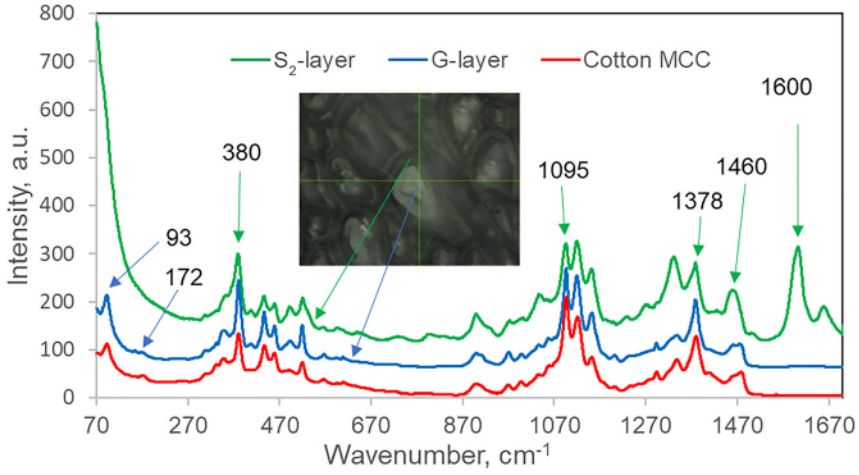

Figure 2: Comparison of 70–1700 cm^{-1} Raman spectra of pure G-layer with pure S_2 and MCC (highly crystalline cellulose, Segal CrI = 89.7%; Agarwal et al. 2021a) (the inset shows the TW regions – G-layer and S_2, from which the shown spectra were obtained). The annotated peaks 93, 172, 380, 1095, 1378, and 1460 cm^{-1} are due to crystalline cellulose, peaks at 380, 1095, 1378, and 1460 cm^{-1} are due to cellulose, and peak 1600 cm^{-1} is due to lignin.

Table 1: CNCs: yield and analysis data.

Sample	Yield (%)	Mean height (nm)	Crystallinity (%) Segal-XRD; 93-Raman; 380-Raman
TW-CNCs	20.7[a]	4.0 ± 1.6	95.5; 69.7; 80.2
OW-CNCs	5.4[a]	3.1 ± 1.4	93.5; 59.2; 73.7
Pulp-CNCs	50.0[b]	4.3 ± 1.4	86.0; 46.4[c]; 55.5[c]

[a]Based on wood holopulp. [b]Based on softwood bleached kraft pulp. [c]Data from Agarwal et al. 2021b.

The CrIs of the three types of CNCs were obtained by Segal-XRD and Raman methods (93- and 380-Raman) (Agarwal et al. 2010, 2018; Ling et al. 2019; Queiroz et al. 2021; Segal et al. 1959). In Table 1, although for a given CNC the value of absolute crystallinity was different between the methods, they all showed the same trend. The high to low CrI order was TW- > OW- > pulp-CNCs (Table 1) indicating that the G-layer derived CNCs were more crystalline compared to the pulp-CNCs. And, irrespective of the CrI estimation-method used, this difference was quite significant (absolute CrI difference between 12 and 19%, Table 1). Lower crystallinity of the pulp-CNCs can be explained by considering that wood-cellulose becomes partly crystalline only during the pulping process (Agarwal et al. 2018), thereby producing lower quality crystalline regions in pulps which, in turn, leads to the CNCs of poor quality. Between the two wood CNCs, TW-CNCs had higher CrI compared to OW-CNCs (more so by the Raman methods than the Segal method, Table 1) and this difference may have originated from the quality of the G-layers. Compared to the OW G-layer, the G-layer in TW is thicker (Figure 4) and may have led to the production of the better CNCs.

3.3 Anatomical analysis

Images of the stained TW and OW cross-sections are shown, respectively, in Figures 4A and B. In Figure 4A, fibers with

Table 2: Chemical composition (%).

Sample	Klason lignin	Glucan	Xylan	Mannan	Arabinan	Galactan	Ratio glucan:xylan[e]
TW	18.3	46.9	13.5	1.0	0.2	0.5	NA[a]
OW	22.2	42.0	15.5	2.6	0.2	0.4	NA
TW holopulp	1.6	61.3	15.2	ND[b]	0.2	ND	78:22
OW holopulp	2.80	49.0	17.5	2.6	0.2	0.3	68:32
Aspen holopulp[c]	3.1	52.3	16.7	1.4	0.3	ND	71:39
SWBKP	0.5	81.3	7.5	5.2	0.3	ND	86:14
Cotton MCC[d]	3.1	92.2	0.1	ND	ND	ND	97:3

[a]Not applicable. [b]Not detected. [c]Reference Agarwal et al. (2013). [d]Reference Agarwal et al. (2017). [e]The amounts of xylan, mannan, arabinan, galactan, and Klason lignin were added and counted as xylan (see text).

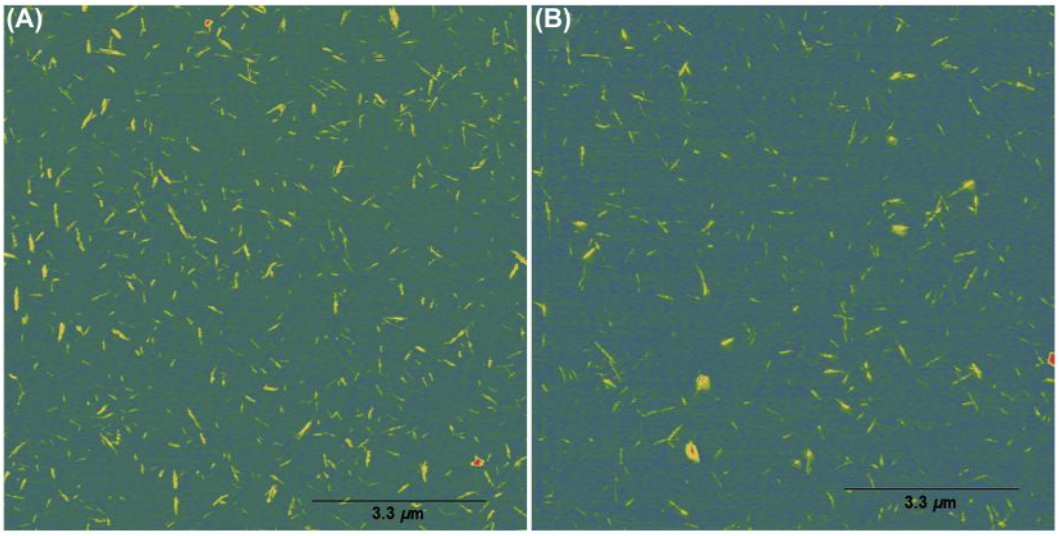

Figure 3: AFM images of (A) TW-CNCs and (B) OW-CNCs. Scale bars: 3.3 µm.

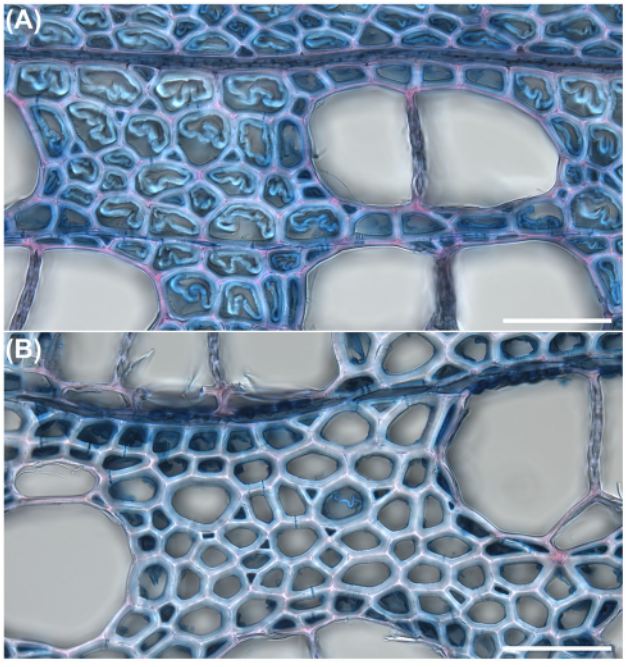

Figure 4: Transmitted light micrographs of transverse sections of aspen stained with alcian blue and safranin O. (A) Tension wood (TW) showing conspicuous gelatinous layers in the great majority of the fibers, and pink-staining cell corners and compound middle lamellae. (B) Opposite wood (OW) showing a fiber with a gelatinous layer, and less prominent pink-staining of cell corners and compound middle lamellae in the fibers, with vessels and vessel-adjacent cells showing stronger pink staining. The blue contents of ray-adjacent fibers are not gelatinous layers. Scale bars: 200 µm.

prominent, thick G-layers (clearly staining blue) represent well over 99% of all fibers; very few fibers without a G-layer over many square millimeters of tissue were observed. Ray cell walls, vessel element cell walls, latest-latewood cells, and fiber CmL showed faint red staining, consistent with lignified tissue when stained with safranin O/alcian blue. The thin, presumed S_1 layers of the gelatinous fiber cell walls were typically hyaline – neither red nor strongly blue. Vessel-adjacent cells sometimes showed some blue-staining cell contents not consistent with a separated G-layer.

On the other hand, surprisingly, OW fibers with G-layers (clearly staining blue) were found although sparsely – less than ~10% of observed fibers. G-layers were typically thin, and the gelatinous fibers were distributed diffusely throughout the growth ring. Normal fiber secondary cell walls showed faint pinkish cast from safranin staining and the cell corners were hyaline to light pink. Vessel-adjacent cells sometimes showed some blue-staining cell contents which was not consistent with a separated G-layer.

3.4 Raman spectra

The intent was to find out how the Raman spectra of various holopulps (TW-, OW-, and aspen Table 2) compare with each other and also with a set of samples prepared by mixing specific amounts of cotton MCC (Whatman CC31, highly crystalline cellulose) and xylan. The results would further help address the question of the presence of crystalline cellulose in normal cell walls of woody tissue. Nine mixture samples of the following MCC:xylan compositional ratios were made – 90:10, 80:20, 70:30, 60:40, 50:50, 40:60, 30:70, 20:80, and 10:90. The purpose was to not only cover the range of possible hemicellulose and Klason lignin contents in the

wood holopulp samples (which in the mixtures is represented by xylan, Table 2), but also to see at what low concentration of cellulose, in the mixture samples, the crystalline-cellulose peaks at 93 and 172 cm^{-1} can no longer be detected. Moreover, could these two bands be detected in the Raman spectra of various holopulps at the glucan:xylan concentrations listed in Table 2. To simplify this, to a first approximation, the holopulps are assumed to be solely made up of cellulose and xylan (i.e., the amounts of xylan, mannan, arabinan, galactan, and Klason lignin were added and counted as xylan, Table 2). This is justifiable considering the fact that, for most of the samples, xylan is the dominant component of the non-glucan constituents and mannan occurs in much smaller amount (Table 2). In case the Raman bands could be detected in the mixture (having similar glucan:xylan composition as in the holopulp) but not in the corresponding holopulp, then it would imply that the cellulose in the holopulp was not as crystalline as the MCC. On the other hand, if the bands were to be detected in both the samples (mixture and the corresponding holopulp), it would imply that the holopulp-cellulose was as crystalline as the MCC.

In Figure 5A, low-frequency (70–550 cm^{-1}) spectra of the holopulps are compared with the spectra of TW-CNCs and SWBKP. Among the holopulps, the spectral peaks at 93 and 172 cm^{-1} were detected, albeit as shoulders, for only TW-holopulp. Moreover, in the spectra of the remaining holopulps, OW-holopulp's contribution at 172 cm^{-1} was hardly noticeable and not perceptible at all at 93 cm^{-1} whereas for the aspen holopulp, none of these bands were noticeable (Figure 5A). In the case of TW-holopulp, the appearance of the features can be explained by the fact that it contained significant amount of crystalline cellulose (G-layer). On the other hand, a much-reduced amount of this layer was present in the OW-holopulp and therefore, the contribution of crystalline cellulose was not evident. Absence of the twin features at 93 and 172 cm^{-1} in the spectra of aspen holopulp argues for the absence of any crystalline cellulose because not only G-layer was absent, but also the cell wall cellulose was not crystalline, as was previously reported (Agarwal et al. 2016, 2018).

Considering the spectra of the MCC:xylan mixtures (Figure 5B), it is clear that peaks at 93 and 172 cm^{-1} are detectable, respectively, up to the MCC:xylan compositional ratios of 40:60 and 60:40. This difference in the detectability of the two bands has to do with the fact that the band at 172 cm^{-1} is much weaker compared to the 93 cm^{-1} band (Figure 5A, TW-CNCs spectrum). In any case, had the cell wall cellulose been highly crystalline in normal cell walls, the holopulp where the glucan:xylan compositional ratio is 71:39 (Table 2), both the bands should have been seen (Figures 5A and B, Table 2). That not being the case, as demonstrated in Figure 5C, the spectra provide evidence in support for the cellulose being not highly crystalline.

3.5 X-ray diffraction

XRDs of tunicin, aspen, amorphous cellulose, and TW-CNCs are shown in Figure 6. Except for the CNCs the information is taken from the authors prior investigations (Agarwal et al. 2013, 2017, 2018, 2021a). Due to its very high crystallinity, tunicin showed the sharpest and most resolved peaks. As expected, compared to tunicin's XRD (Figure 6A), the diffractogram of TW-CNCs is less resolved, most likely due to the smaller size of its crystals in relation to that of tunicin's. But the diffractogram is still quite strong, as was expected based on the Raman spectrum of the G-layer (Figure 2). However, important to note in Figure 6A are the significantly weaker and broader characteristics of the diffraction pattern of wood where (1–10) and (110) peaks remained completely unresolved and (200) peak was rather broad. If indeed the wood-cellulose was crystalline, an XRD similar to that of TW-CNCs would have been obtained, which was clearly not the case. Moreover, between TW-CNCs and wood cellulose, the fibril/crystal size difference does not exist because both are approximately 3 nm wide (Table 1) (Agarwal et al. 2021b; Saito et al. 2007). And therefore, although the effect of cellulose crystal size on XRD has been reported in the literature (French and Cintron 2013), when comparing the two XRDs (Figure 6A), effect of fibril/crystal-size on the wood XRD does not apply. However, further considering that in cell walls ~15 nm wide cellulose microfibril bundles exist (Abe et al. 2007), the increased bundle size compared to 3 nm wide fibrils is likely to produce narrower peaks in the XRD. This is likely due to the increased order at the interface of the combined fibrils where the cellulose chains have lower deformation flexibility. Moreover, microfibril shape (Newman et al. 2013) is also not likely to be a factor because under this scenario, fibrils are still crystalline and therefore, a 93 cm^{-1} peak in Raman spectroscopy should have been seen. Consequently, most likely, the width of the wood XRD originates from the fact that the cellulose is not crystalline. The difference between the XRDs of wood and amorphous cellulose is shown in Figure 6B and clearly, in many regions of 2θ the contributions overlap, if not similar. Therefore, in the view of the authors, an aggregated phase of cellulose in wood that is non-crystalline but organized/aligned in some fashion, is likely to produce such a diffractogram. This hypothesis is supported by the fact that water induced reorganization of cellulose gives rise to increased contributions at 2θ positions where crystalline cellulose also

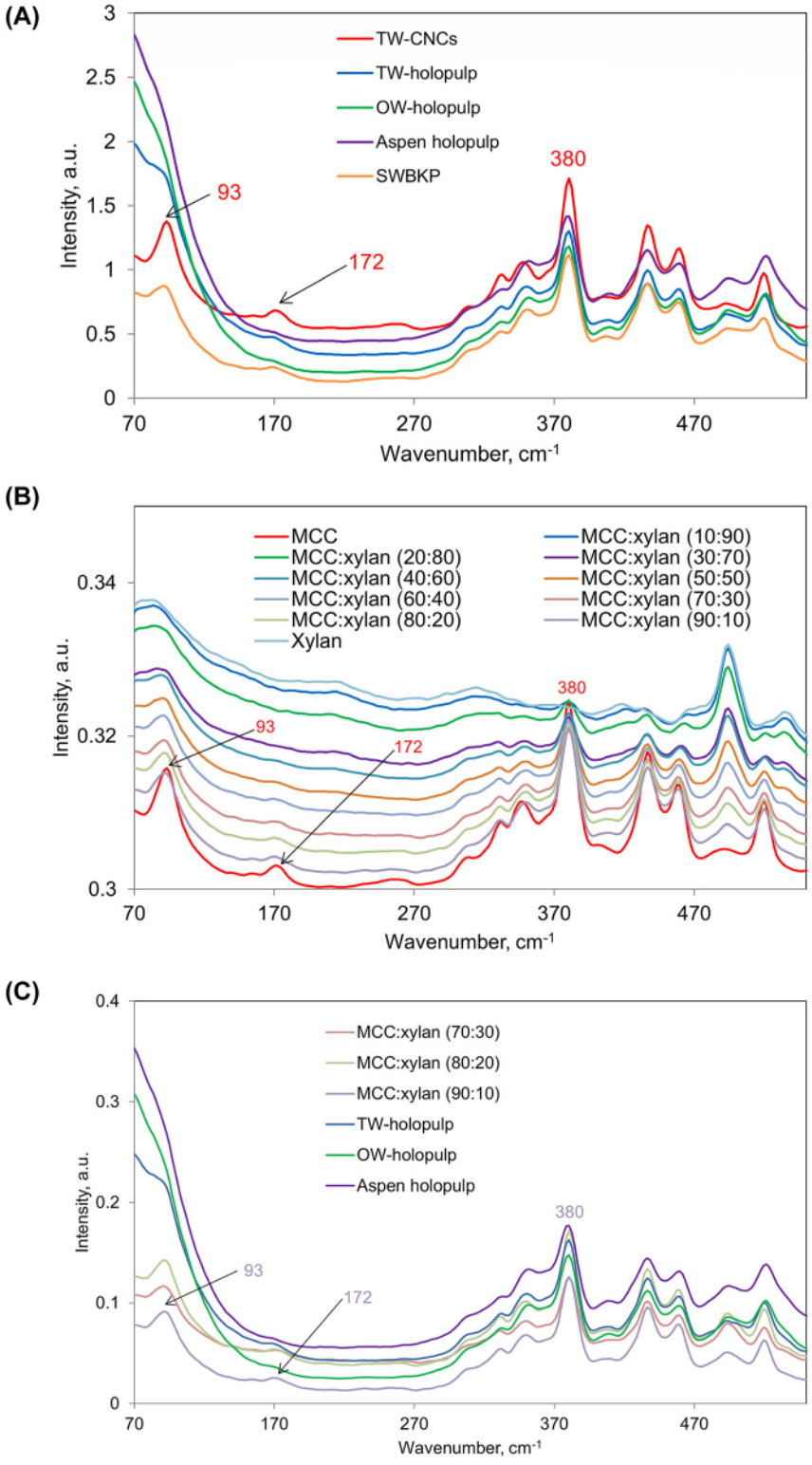

Figure 5: Raman spectra of samples. (A) Raman spectra of three holopulps, SWBKP, and TW-CNCs. (B) Raman spectra of mixtures of MCC:xylan at various compositions. (C) Comparison of the spectra of various holopulps and the appropriate MCC:xylan mixtures (70:30, 80:20, and 90:10). The annotated peaks in Figure 5A–C are, respectively, from TW-CNCs, MCC, and MCC:xylan (90:10).

contributes (Agarwal et al. 2017, 2021a). Due to this organization, compared to amorphous cellulose, the long-range order increases and as seen in Figure 6B, stronger contributions are likely to be generated in 2θ regions 14–17° and 21–24°. Additionally, based on to the classic Bragg scattering (Equation (4)), in a non-crystalline solid, as the distance between molecular scattering entities changes (d is variable as the interatomic distance changes in a sample) scattering

angle θ and therefore, the positions of the intensity contributions also vary, thus giving rise to the broadness of the wood-cellulose XRD (Figure 6B). Accordingly, the XRD data analysis further supported the non-crystalline nature of wood cellulose.

$$\lambda = 2d \sin\theta \quad (4)$$

4 Supported model

Findings of this investigation support the model of wood-cellulose previously proposed by the authors of this paper (Agarwal et al. 2016, 2018). Under that model, a cross sectional view of which is depicted in Figure 7, water has access to the interior chains of a cellulose fibril. It is further proposed that water plays a structuring role within the fibril whereupon the assembled structure of the fibril resembles that of cellulose I, nevertheless, the fibril remains non-crystalline. This is likely, considering that water molecules that are in the proximity of cellulose partially loose the tetrahedral ordering (as in bulk water) and can participate in the H-bond network which results in the ordering of the cellulose (Paolantoni et al. 2007). This non-crystalline option for the cellulose was reinforced by the obtained spectroscopic and diffractometric data (e.g., by IR, Raman, and XRD) where it has been demonstrated that cellulose's non-crystalline state is capable of making contributions in the regions where the crystalline form contributes (although there are certain exceptions, e.g., contributions at 93 and 172 cm^{-1} peaks in Raman spectroscopy) (Agarwal et al. 2021a). Particularly, in the case of ball-milled MCC, it was observed that when such cellulose samples were wet with water, most underwent conformational changes at the molecular level and these changes gave rise to increased contributions in spectral and diffraction regions typically associated with the contributions of cellulose I. Indeed, the water-induced organization of amorphous

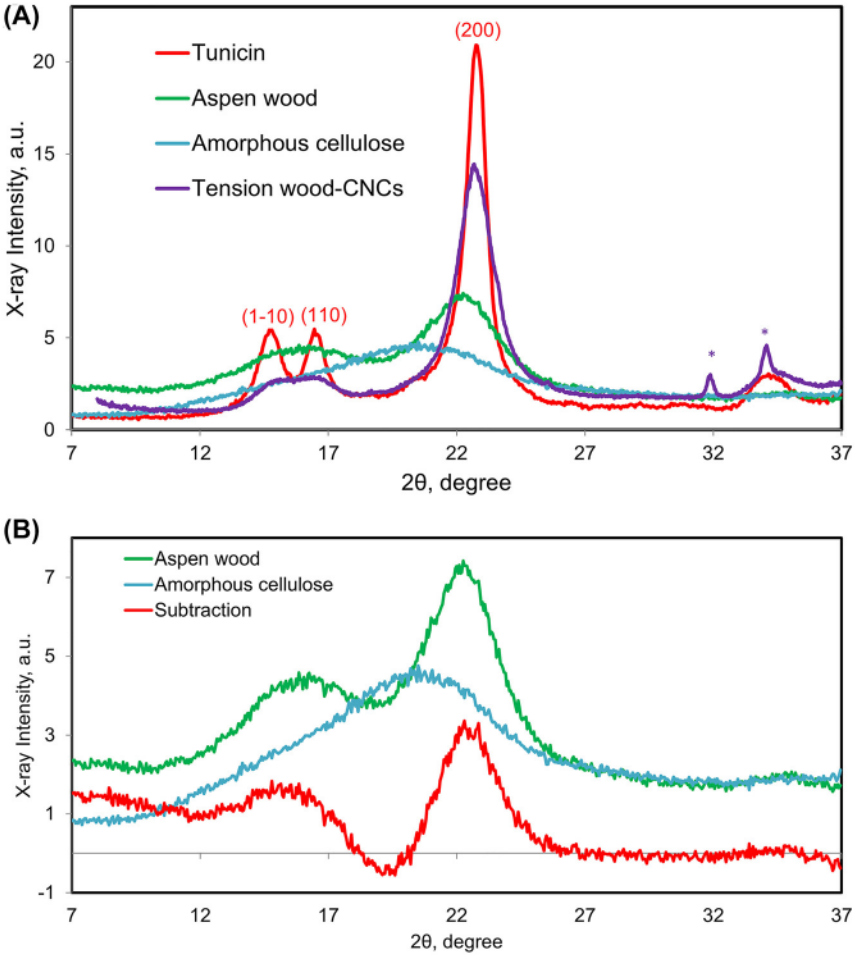

Figure 6: XRDs of samples. (A) Comparison of XRDs of amorphous cellulose, aspen wood, TW-CNCs, and tunicin. (B) Result of subtraction of the XRDs (aspen wood – amorphous cellulose). In (A) peaks marked with * are due to Na_2SO_4 impurity and the annotated peaks are of tunicin.

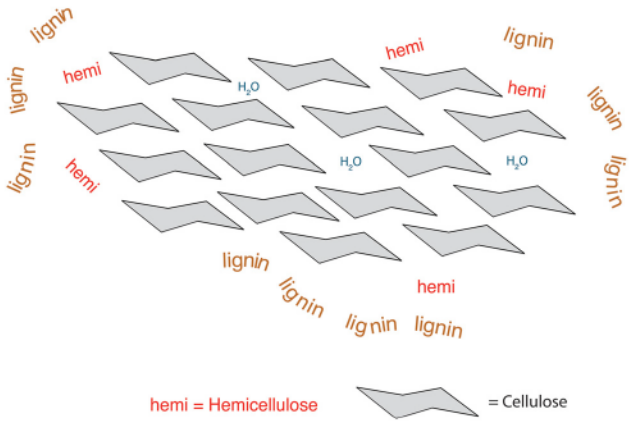

Figure 7: Cross-sectional view of the proposed non-crystalline model of wood-cellulose.

cellulose resulted in 78.5% increase in Segal-crystallinity (Agarwal et al. 2021a). A cross-sectional view of the previously reported non-crystalline model is portrayed in Figure 7.

5 Conclusions

In this study, to understand the nature of wood cellulose in native state, further research using tension aspen wood was carried out. All of the obtained results supported the earlier reported finding that wood cellulose is not crystalline. Raman spectra obtained from distinct S_2 and G-layer regions of TW suggested that the spectrum of the former lacked a crystallinity-specific band at 93 cm^{-1} which was present in the G-layer. When the G-layer rich TW was hydrolyzed by 64% H_2SO_4, CNCs were obtained and therefore, obviously, such a treatment did not destroy the crystalline cellulose. On the other hand, the yield of the CNCs from the opposite wood was very low due to the fact that such wood contained very little G-layer. The acid hydrolysis data obtained here clearly supported the earlier finding that when untreated softwood is hydrolyzed by the 64% H_2SO_4, no CNCs were produced. Other analysis that consisted of comparing the Raman spectra of various wood-holopulps with those of the mixtures of crystalline-cellulose and xylan at compositions representative of the holopulps indicated that except in the case of TW-holopulp, the spectra of the holopulps lacked the crystalline cellulose features at 93 and 172 cm^{-1}. Similarly, the XRD analysis of four materials – amorphous cellulose, aspen wood, TW-CNCs, and tunicin, provided further support to the view that, in the native state, cell wall cellulose is non-crystalline.

Acknowledgments: The authors are very thankful to Alex Wiedenhoeft (Wood Anatomy and Forest Mycology Group, FPL) for carrying out the anatomical analysis of the wood samples. The authors gratefully acknowledge the use of X-ray facilities and instrumentation supported by NSF through the University of Wisconsin Materials Research Science and Engineering Center (DMR-1121288).
Author contributions: All the authors accept responsibility for the entire content of this manuscript and approve its submission.
Research funding: None declared.
Conflict of interest statement: The authors declare that they have no known competing financial interests or personal relationships that could have influenced the work reported in this manuscript.

References

Abe, K., Iwamoto, S., and Yano, H. (2007). Obtaining cellulose nanofibers with a uniform width of 15 nm from wood. Biomacromolecules 8: 3276–3278.
Agarwal, U.P. (2006). Raman imaging to investigate ultrastructure and composition of plant cell walls: distribution of lignin and cellulose in black spruce wood (Picea mariana). Planta 224: 1141–1153.
Agarwal, U.P. (2014). 1064 nm FT-Raman spectroscopy for investigations of plant cell walls and other biomass materials. Front. Plant Sci. 5: 490.
Agarwal, U.P., Reiner, R.S., and Ralph, S.A. (2010). Cellulose I crystallinity determination using FT–Raman spectroscopy: univariate and multivariate methods. Cellulose 17: 721–733.
Agarwal, U.P., McSweeny, J.D., and Ralph, S.A. (2011). FT–Raman investigation of milled-wood lignins: softwood, hardwood, and chemically modified black spruce lignins. J. Wood Chem. Technol. 31: 324–344.
Agarwal, U.P., Reiner, R.S., and Ralph, S.A. (2013). Estimation of cellulose crystallinity of lignocelluloses using near-IR FT-Raman spectroscopy and comparison of the Raman and Segal-WAXS methods. J. Agric. Food Chem. 61: 103–113.
Agarwal, U.P., Ralph, S.A., Reiner, R.S., Moore, R.K., and Baez, C. (2014). Impacts of fiber orientation and milling on observed crystallinity in jack pine. Wood Sci. Technol. 48: 1213–1227.
Agarwal, U.P., Ralph, S.A., Reiner, R.S., and Baez, C. (2016). Probing crystallinity of never-dried wood cellulose with Raman spectroscopy. Cellulose 23: 125–144.
Agarwal, U.P., Ralph, S.A., Baez, C., Reiner, R.S., and Verrill, S.P. (2017). Effect of sample moisture content on XRD-estimated cellulose crystallinity index and crystallite size. Cellulose 24: 1971–1924.
Agarwal, U.P., Ralph, S.A., Reiner, R.S., and Baez, C. (2018). New cellulose crystallinity estimation method that differentiates between organized and crystalline phases. Carbohydr. Polym. 190: 262–270.
Agarwal, U.P., Ralph, S.A., Baez, C., and Reiner, R.S. (2021a). Contributions of crystalline and noncrystalline cellulose can occur in the same spectral regions: evidence based on Raman and IR and its implication for crystallinity measurements. Biomacromolecules 22: 1357–1373.

Agarwal, U.P., Reiner, R.S., Ralph, S.A., Catchmark, J., Chi, K., Foster, E.J., Hunt, C.G., Baez, C., Ibach, R.E., and Hirth, K.C. (2021b). Characterization of the supramolecular structures of cellulose nanocrystals of different origins. Cellulose 28: 1369–1385.

Andersson, S., Serimaa, R., Paakkari, T., Saranpaa, P., and Pesonen, E. (2003). Crystallinity of wood and the size of cellulose crystallites in Norway spruce (Picea abies). J. Wood Sci. 49: 531–537.

Atalla, R.H., Atalla, R.S., and Agarwal, U.P. (2017). The nanostructures of native celluloses, their transformations upon isolation, and their implications for production of nanocelluloses. In: Agarwal, U.P., Atalla, R.H., and Isogai, A. (Eds.), *Nanocelluloses: their preparation, properties, and applications. ACS Symposium Series*. American Chemical Society, Washington, DC, pp. 1–18.

Chen, L., Wang, Q., Hirth, K., Baez, C., Agarwal, U.P., and Zhu, J.Y. (2015). Tailoring the yield and characteristics of wood cellulose nanocrystals (CNC) using concentrated acid hydrolysis. Cellulose 22: 1753–1762.

Coutand, C., Jeronimidis, G., Chanson, B., and Loup, C. (2004). Comparison of mechanical properties of tension and opposite wood in Populus. Wood Sci. Technol. 38: 11–24.

Cresswell, R., Dupree, R., Brown, S.P., Pereira, C.S., Skaf, M.S., Sorieul, M., Dupree, P., and Hill, S. (2021). Importance of water in maintaining softwood secondary cell wall nanostructure. Biomacromolecules 22: 4669–4680.

Dadswell, H.E. and Wardrop, A.B. (1955). The structure and properties of tension wood. Holzforschung 9: 97–103.

Davis, M.W. (1998). A rapid method for compositional carbohydrate analysis of lignocellulosics by high pH anion-exchange chromatography with pulse amperometric detection (HPAE/PAD). J. Wood Chem. Technol. 18: 235–252.

Fernandes, A.N., Thomas, L.H., Altaner, C.M., Callow, P., Forsyth, V.T., Apperley, D.C., Kennedy, C.J., and Jarvis, M.C. (2011). Nanostructure of cellulose microfibrils in spruce wood. Proc. Natl. Acad. Sci. USA 108: E1195–E1203.

French, A.D. and Cintron, M.S. (2013). Cellulose polymorphy, crystallite size, and the Segal crystallinity index. Cellulose 20: 583–588.

Funaki, C., Toyouchi, T., Hoshina, H., Ozaki, Y., and Sato, H. (2017). Terahertz imaging of the distribution of crystallinity and crystalline orientation in a poly(e-caprolactone) film. Appl. Spectrosc. 71: 1537–1542.

Gao, J., Jebrane, M., Terziev, N., and Daniel, G. (2021). Enzymatic hydrolysis of the gelatinous layer in tension wood of Salix varieties as a measure of accessible cellulose for biofuels. Biotechnol. Biofuels 14: 141.

Guerriero, G., Fugelstad, J., and Bulone, V. (2010). What do we really know about cellulose biosynthesis in higher plants? J. Integrative Plant Biol. 52: 161–175.

Hill, S.J., Kirby, N.M., Mudie, S.T., Hawley, A.M., Ingham, B., Franich, R.A., and Newman, R.H. (2010). Effect of drying and rewetting of wood on cellulose molecular packing. Holzforschung 64: 421–427.

Jarvis, M.C. (2018). Structure of native cellulose microfibrils, the starting point for nanocellulose manufacture. Phil. Trans. Math. Phys. Eng. Sci. 376: 20170045.

Kontturi, E., Meriluoto, A., Penttila, P.A., Baccile, N., Malho, J.-M., Potthast, A., Rosenau, T., Ruokolainen, J., Serimaa, R., Laine, J., et al. (2016). Degradation and crystallization of cellulose in hydrogen chloride vapor for high-yield isolation of cellulose nanocrystals. Angew. Chem. Int. Ed. 55: 14455–14458.

Kuribayashi, T., Ogawa, Y., Rochas, C., Matsumoto, Y., Heux, L., and Nishiyama, Y. (2016). Hydrothermal transformation of wood cellulose crystals into pseudo-orthorhombic structure by cocrystallization. ACS Macro Lett. 5: 730–734.

Larsson, P.T., Wickholm, K., and Iversen, T. (1997). A CP/MAS 13C NMR investigation of molecular ordering in celluloses. Carbohydr. Res. 302: 19–25.

Leboucher, J., Bazin, P., Goux, D., Siblani, H.E., Travert, A., Barbulée, A., Bréard, J., and Duchemin, B. (2020). High-yield cellulose hydrolysis by HCl vapor: co-crystallization, deuterium accessibility and high-temperature thermal stability. Cellulose 27: 3085–3105.

Leppanen, K., Andersson, S., Torkkeli, M., Knaapila, M., Kotelnikova, N., and Serimaa, R. (2009). Structure of cellulose and microcrystalline cellulose from various wood species, cotton and flax studied by X-ray scattering. Cellulose 16: 999–1015.

Ling, Z., Wang, T., Makarem, M., Cintron, M.S., Cheng, H.N., Kang, X., Bacher, M., Potthast, A., Rosenau, T., King, H., et al. (2019). Effects of ball milling on the structure of cotton cellulose. Cellulose 26: 305–328.

Makarem, M., Lee, C.M., Kafle, K., Huang, S., Chae, I., Kim, S.H., and Kubicki, J.D. (2019). Probing cellulose structures with vibrational spectroscopy. Cellulose 26: 35–79.

Mellerowicz, E.J., Baucher, M., Sundberg, B., and Boerjan, W. (2001). Unraveling cell wall formation in the woody dicot stem. Plant Mol. Biol. 47: 239–274.

Mellerowicz, E.J., Immerzeel, P., and Hayashi, T. (2008). Xyloglucan: the molecular muscle of trees. Ann. Bot. 102: 659–665.

Moon, R.J., Martini, A., Nairn, J., Simonsen, J., and Youngblood, J. (2011). Cellulose nanomaterials review: structure, properties and nanocomposites. Chem. Soc. Rev. 40: 3941–3994.

Muller, M., Burghammer, M., and Sugiyama, J. (2006). Direct investigation of the structural properties of tension wood cellulose microfibrils using microbeam X-ray fiber diffraction. Holzforschung 60: 474–479.

Nam, S., French, A.D., Condon, B.D., and Concha, M. (2016). Segal crystallinity index revisited by the simulation of X-ray diffraction patterns of cotton cellulose Iβ and cellulose II. Carbohydr. Polym. 135: 1–9.

Nazhad, M.M. and Paszner, L. (1994). Fundamentals of strength loss in recycled paper. Tappi J. 77: 171–179.

Newman, R.H. (2004). Carbon-13 NMR evidence for cocrystallization of cellulose as a mechanism for hornification of bleached kraft pulp. Cellulose 11: 45–52.

Newman, R.H., Hill, S.J., and Harris, P.J. (2013). Wide-angle X-ray scattering and solid-state nuclear magnetic resonance data combined to test models for cellulose microfibrils in mung bean cell walls. Plant Physiol. 163: 1558–1567.

Ono, Y., Takeuchi, M., and Isogai, A. (2022). Characterization of solid-state structures, molar masses, and microfibril structures of cellulose in never-dried cotton fibers and ramie bast fibers. Cellulose 29: 9105–9119.

Paolantoni, M., Sassi, P., Morresi, A., and Santini, S. (2007). Hydrogen bond dynamics and water structure in glucose-water solutions by depolarized Rayleigh scattering and low frequency Raman spectroscopy. J. Chem. Phys. 127: 024504.

Park, S., Johnson, D.K., Ishizawa, C.I., Parilla, P.A., and Davis, M.F. (2009). Measuring the crystallinity index of cellulose by solid state 13C nuclear magnetic resonance. Cellulose 16: 641–647.

Parrott, E.P.J. and Zeitler, J.A. (2015). Terahertz time-domain and low-frequency Raman spectroscopy of organic materials. Appl. Spectrosc. 69: 1–25.

Penttila, P.A., Altgen, M., Carl, N., van der Linden, P., Morfin, I., Osterberg, M., Schweins, R., and Rautkari, L. (2020). Moisture-related changes in the nanostructure of woods studied with X-ray and neutron scattering. Cellulose 27: 71–87.

Phanthong, P., Reubroycharoen, P., Hao, X., Xu, G., Abudula, A., and Guan, G. (2018). Nanocellulose: extraction and application. Carbon Resour. Convers. 1: 32–43.

Pilate, G., Dejardin, A., Laurans, F., and Leple, J.-C. (2004). Tension wood as a model for functional genomics of wood formation. New Phytol. 164: 63–72.

Queiroz, A.L.P., Kerins, B.M., Yadav, J., Farag, F., Faisal, W., Crowley, M.E., Lawrence, S.E., Moynihan, H.A., Healy, A.-M., Vucen, S., et al. (2021). Investigating microcrystalline cellulose crystallinity using Raman spectroscopy. Cellulose 28: 8971–8985.

Ramanen, P., Penttila, P.A., Svedstrom, K., Maunu, S.L., and Serimaa, R. (2012). The effect of drying method on the properties and nanoscale structure of cellulose whiskers. Cellulose 19: 901–912.

Saito, T., Kimura, S., Nishiyama, Y., and Isogai, A. (2007). Cellulose nanofibers prepared by TEMPO-mediated oxidation of native cellulose. Biomacromolecules 8: 2485–2491.

Sannigrahi, P., Ragauskas, A.J., and Miller, S.J. (2008). Effects of two-stage dilute acid pretreatment on the structure and composition of lignin and cellulose in loblolly pine. Bioenergy Res. 1: 205–214.

Segal, L., Creely, J.J., Martin, A.E., and Conrad, C.M. (1959). An empirical method for estimating the degree of crystallinity of native cellulose using the x-ray diffractometer. Text. Res. J. 29: 786–794.

Spiliopoulos, P., Spirk, S., Pääkkönen, T., Viljanen, M., Svedström, K., Pitkänen, L., Awais, M., and Kontturi, E. (2021). Visualizing degradation of cellulose nanofibers by acid hydrolysis. Biomacromolecules 22: 1399–1405.

TAPPI test method (1983). *Acid insoluble lignin in wood and pulp; official test method T-222 (Om)*. TAPPI, Atlanta.

Thomas, L.H., Forsyth, V.T., Šturcová, A., Kennedy, C.J., May, R.P., Altaner, C.M., Apperley, D.C., Wess, T.J., and Jarvis, M.C. (2013). Structure of cellulose microfibrils in primary cell walls from collenchyma. Plant Physiol. 161: 465–476.

Toba, K., Yamamoto, H., and Yoshida, M. (2013). Crystallization of cellulose microfibrils in wood cell wall by repeated dry-and-wet treatment, using X-ray diffraction technique. Cellulose 20: 633–643.

Toba, K., Nakai, T., Kanbayashi, T., and Saito, H. (2022). Effects of cyclic drying and moistening on the mechanical and physical properties of wood. Eur. J. Wood Wood Prod. 80: 1333–1341.

van de Ven, T.G.M. and Sheikhi, A. (2016). Hairy cellulose nanocrystalloids: a novel class of nanocellulose. Nanoscale 8: 15101–15114.

Vieira, F.S. and Pasquini, C. (2014). Determination of cellulose crystallinity by terahertz time domain spectroscopy. Anal. Chem. 86: 3780–3786.

Wada, M., Okano, T., Sugiyama, J., and Horii, F. (1995). Characterization of tension and normally lignified wood cellulose in Populus maximowiczii. Cellulose 2: 223–233.

Wang, T., Yang, H., Kubicki, J.D., and Hong, M. (2016). Cellulose structural polymorphism in plant primary cell walls investigated by high-field 2D solid-state NMR spectroscopy and density functional theory calculations. Biomacromolecules 17: 2210–2222.

Wang, H., Tsuchikawa, S., and Inagaki, T. (2021). Terahertz time-domain spectroscopy as a novel tool for crystallographic analysis in cellulose: the potentiality of being a new standard for evaluating crystallinity. Cellulose 28: 5293–5304.

Yamamoto, H., Ruelle, J., Arakaw, Y., Yoshid, M., Clair, B., and Gril, J. (2010). Origin of the characteristic hygro-mechanical properties of the gelatinous layer in tension wood from Kunugi oak (Quercus acutissima). Wood Sci. Technol. 44: 149–163.

Zabler, S., Paris, O., Burgert, I., and Fratzl, P. (2010). Moisture changes in the plant cell wall force cellulose crystallites to deform. J. Struct. Biol. 171: 133–141.

Zhu, J.Y., Agarwal, U.P., Ciesielski, P.N., Himmel, M.E., Gao, R., Deng, Y., Morits, M., and Österberg, M. (2021). Towards sustainable production and utilization of plant-biomass-based nanomaterials: a review and analysis of recent developments. Biotechnol. Biofuels 14: 114.